

Chapter 7

The channel with antidots

This chapter studies the longitudinal magnetoconductance of a mesoscopic channel with a central antidot dimer. The experimentally observed conductance oscillates in dependence of both the magnetic field strengths and the antidot radius (regulated by the applied gate voltage). The period of the oscillations in B is approximately constant, and the maxima positions exhibit characteristic dislocations when varying the antidot diameter. This behavior was previously related to inherent quantum effects and believed not to be accessible by semiclassical methods. The semiclassical description developed in this chapter is able to reproduce qualitatively as well as quantitatively all observed features. Additionally, it allows an intuitive explanation of the origin of the maxima dislocations.

Contents

7.1	The device	70
7.2	Experimental results	71
7.3	Theoretical description	72
7.3.1	Intuitive discussion	72
7.3.2	Quantum mechanical calculation	73
7.4	Semiclassical description of the conductance	74
7.4.1	Landauer-Büttiker or Kubo?	75
7.4.2	The model potential	75
7.4.3	The periodic orbits	76
7.4.4	Evaluating the trace formula	78
7.4.4.1	Numerical implementation of the uniform approximation	78
7.4.4.2	The influence of the bifurcations	78
7.5	Semiclassical results	80
7.5.1	Fourier components of the quantum oscillations	80
7.5.2	The conductance variation with B	81
7.5.3	The maximum spacing	83
7.5.4	Variation of the antidot diameter	84
7.6	Semiclassical interpretation	85
7.7	Summary	87

Many physical observations in mesoscopic ballistic devices could successfully be explained by the interference of classical orbits in the system. Among these are the Shubnikov-de-Haas oscillations and the QHE of the free 2DEG discussed in the previous chapter, the magnetoconductance oscillations of a 2DEG in an antidot superlattice [84, 55] and those of a large circular quantum dot [62]. Also the current oscillations in a resonant tunneling diode (RTD) [114] could be described in these terms. There is, however, an ongoing discussion which effects can be treated using semiclassical methods, and which are of genuine quantum origin (i. e. of higher than leading order in \hbar).

The experimental observations of a mesoscopic channel with a central antidot molecule (a dimer) have been reproduced by a quantum calculation [48]. The authors related the measured magnetoconductance features to inherent quantum effects. They therefore claimed that the features are not accessible by semiclassical approximations. This motivates a more detailed examination whether the observations of this system are really beyond the limit of a semiclassical description.

A second reason for working out a semiclassical approximation of this structure is that it has a mixed phase space. The bifurcations which occur in those systems lead to divergencies in a leading-order \hbar approximation. Much interest has been focused on the implementation of bifurcations in semiclassical approximations (see for example Ref. [71] and the references cited therein) and to track down their influence on experimental quantum oscillations. In the RTD, for example, period-doubling bifurcations were found to be responsible for a period doubling in the oscillations of the observed I-V curves [114]. The examination of the channel system will, as it exhibits bifurcations, contribute to this discussion.

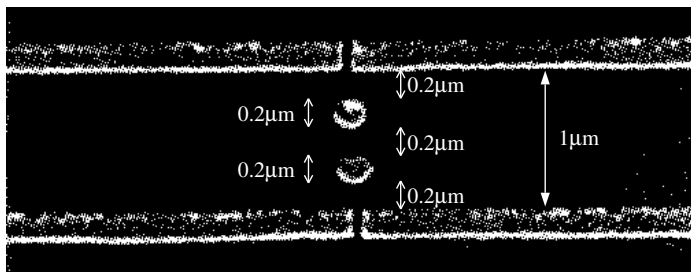
Finally, the quantum calculations for the channel were able to reproduce its main features. They are, however, numerically so demanding that the dependence on the external variables could only be varied on a relatively coarse grid. For semiclassical calculations these restrictions will be considerably less tight. Within such a description, even a fit of the effective potential of the system could be feasible.

These three points make the channel system a real challenge to semiclassics.

7.1 The device

The device consists of electrostatic gates confining a high-mobility 2DEG in a GaAs/GaAlAs heterostructure. The 2DEG was 82nm beneath the surface, its electron density was $n_e \approx 3.47 \times 10^{15} m^{-2}$, and the mobility about $100 m^2 V^{-1} s^{-1}$. The SEM picture of the

Figure 7.1: *SEM photograph of the gate structure. All gates were contacted separately in a later step. For the experiments discussed in this work, all channel gates are connected to the common gate voltage V_g , and the two antidots are biased with V_d .*



gate structure is shown in Fig. 7.1. Four metallized gates are used to define a long, narrow channel ($5 \mu m \times 1 \mu m$). Two circular gates with a diameter of $0.2 \mu m$ at a distance of $0.2 \mu m$

from each other and from the channel gates define the antidot dimer. All gates are individually contacted using a bridge technique. Details about the device and its fabrication are presented in [33, 48, 34] and the references cited therein. All measurements were taken at $T \approx 100\text{mK}$ using standard low-excitation AC-techniques. The magnetic field was applied perpendicular to the 2DEG.

7.2 Experimental results

This extremely versatile device was used for a variety of different experiments. The conductance was examined for the channel (using all four channel gates) and the half channel (using only the left channel gates). The antidot gate voltages were varied from the open channel to complete pinch-off, and the magnetic field range examined stretches from zero field to the high-field regime, where the quantum mechanical edge channel picture gets accurate. Applying gate voltages that pinch off all but one constriction establishes a quantum point contact (QPC) in the system. A lot of work was dedicated to the measurement of the quantized conductance effects of these QPCs. The corresponding experimental plateaus were also used to approximately scale the antidot voltages to an effective depletion width of both the antidots and the channel walls. Details on these experiments can be found in Refs. [34, 33, 35, 48, 47, 67].

For the experiments considered in this work, an identical voltage V_g , which was held fixed, was applied to all channel gates. Both antidot gates were given the same bias voltage V_d , which was the second parameter besides the magnetic field. The parameter range of interest for this thesis corresponds to large antidots which overlap, so that the central constriction is pinched off. The magnetic field is varied in the regime where the cyclotron diameter of the classical electron motion is comparable with the channel width. In the following, a short summary of the experimental findings relevant for this work will be given.

Fig. 7.2(a) shows a typical magnetoconductance trace measured for large antidots. The longitudinal conductance G_{xx} is near 4 conductance units e^2/h for most field strengths, dropping to approximately half the value in a sharp peak. The peak position corresponds to the commensurability of the size of the antidot dimer and the classical cyclotron diameter (marked with arrows)¹. Note that this is completely analogous to the commensurability peaks observed in antidot lattices [84, 55]. Fig. 7.2(b) gives a closeup of the peak (boxed region in (a)). Superimposed on the peak, quantum oscillations with an approximately constant period can be observed. This is studied in more detail in (c), where the spacings of the neighboring conductance maxima are plotted as a function of B . The different curves correspond to slightly different antidot voltages. The average spacing of the maxima is nearly constant, only slightly decreasing with stronger fields. Superimposed on this smooth trend random like variations are observed.

The unique design of the sample with individually contacted gates allows to change the voltages of the antidots without affecting the other system properties. This was exploited to measure the influence of the antidot diameter, which is directly related to the applied voltage via the induced depletion width. Fig. 7.2(d) shows the influence of this parameter. The points in the diagram correspond to the positions of the maximum of G_{xx} , the solid

¹The antidot size is determined by the lowest point of the saddle of the model potential (defined below in Eq. (7.1), with $s_d = 2$ and $s_g = 1$).

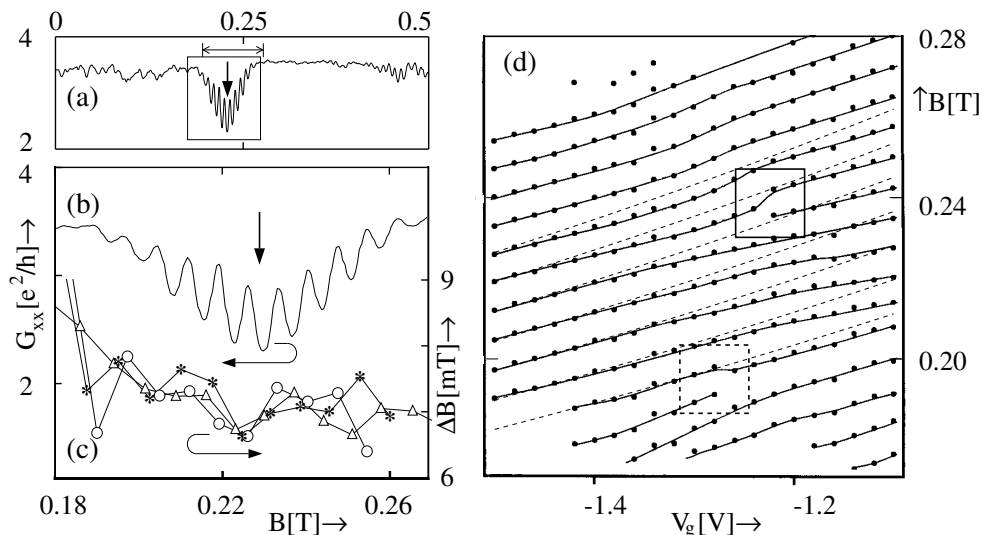


Figure 7.2: *Experimental results. (a,b) Magnetoconductance trace for $V_g = -1.44$ V. The vertical arrows indicate the commensurability condition (see main text). (c) Spacing of the conductance maxima for three gate voltages $V_g = -1.42 \dots -1.5$ V. (d) Dots correspond to the positions of the conductance maxima in dependence of B and V_g . Solid lines are to guide the eye. Dashed lines are calculated from the simple picture described in Sec. 7.3.1.*

lines are just to guide the eye. For smaller antidot voltage the maxima move to stronger fields. They shift mostly parallel, interrupted by characteristic dislocations (boxes).

7.3 Theoretical description

7.3.1 Intuitive discussion

Some of the observed effects can immediately be understood on an intuitive level. A simple picture will clarify which of the features need more detailed discussion.

Since the central constriction is pinched off in the observed regime of antidot voltages, two QPCs are formed between the channel wall and the antidots. The first plateau of quantized conduction leads to a conductance of e^2/h per constriction and per spin, so that the value of $4e^2/h$ is expected if no interference takes place between the QPCs. If the cyclotron diameter equals the channel width, the electrons passing the lower constriction can be focused back through the upper constriction, so that the conductance falls to $2e^2/h$. Using the simple model potential defined below in Eq. (7.1), one can estimate the central peak position by assuming that the orbits are cyclotron-like, passing the saddle of the potential at the lowest point. A rough estimate of the peak width is given by the magnetic field strengths where cyclotron orbits pass the constriction at Fermi energy. These estimates are compared to the experimental G_{xx} in Fig. 7.2(a). The magnitude of the conductance, the position of the conductance dip (vertical arrow), and also its width (horizontal arrow) are in quantitative agreement with this simple consideration.

The oscillations superimposed on the peak may be explained in analogy to the Aharonov-Bohm (AB) effect. Identifying cyclotron orbits around the two central antidots with the AB ring, equidistant maxima in B are expected. Subsequent maxima correspond in

this picture to an additional flux quantum through the ring, so that their spacing only depends on the ring area. The experimentally observed $\Delta B \approx 7\text{mT}$ (cf. Fig. 7.2(c)) corresponds to a diameter of the AB ring of $\approx 0.86\mu\text{m}$. This is consistent with the device dimensions extracted from the SEM photograph Fig. 7.1. Following this interpretation further, the conductance maxima are expected to shift to larger B fields if the antidot diameter is decreased. Taking the approximate scaling between V_g and depletion with s_d from Kirczenow *et al.* [48] allows a quantitative calculation of the expected effect.² The prediction of this simple model is shown in Fig. 7.2(d) with dashed lines. Considering the crude approximations made, the agreement with the experiment is remarkable.³

The questions which remain to be answered by a more detailed analysis concern the deviations from this simple behavior: (1) How does the spacing of the maxima change with B ? (2) Which mechanism is responsible for the dislocations of the maxima positions?

7.3.2 Quantum mechanical calculation

Kirczenow *et al.* [48] presented a quantum mechanical calculation using a transfer matrix technique on a lattice. The model potential both for the channel and the antidot gates was chosen⁴ as

$$V(r) = \begin{cases} E_F [r/a_0 - (1+s)]^2 & \text{for } r < a_0(1+s) \\ 0 & \text{otherwise} \end{cases}, \quad (7.1)$$

with $a_0 = 0.05\mu\text{m}$. Here r denotes the distance to the gate, and a_0 the length scale over which the potential falls off from E_F to 0, i.e. the diffuseness of the potential. s is a dimensionless parameter modeling the depletion width around the gates. For the gates defining the channel, $s = s_c = 1$ was used unless otherwise noticed. The conductance was obtained from the Landauer formula $g = (e^2/h)\text{Tr}(\mathbf{t}\mathbf{t}^\dagger)$. The calculations were performed for $T = 0$ and neglecting impurity scattering. Therefore the quantum mechanical approach misses a smoothing of the data due to temperature and impurity effects.

The results relevant for the further discussion are reproduced in Fig. 7.3. (a) shows the magnetoconductance trace, (b) the variation of the maxima spacings, and (c) the positions of the maxima with varying antidot diameter. The quantum mechanical calculation (heavy lines) qualitatively reproduces both the saturation of the peak spacings and the maxima dislocations observed experimentally. Characteristic deviations are the shift of the conductance peak to higher B-fields, and correspondingly a shift of the ΔB versus B

²To establish a relation between the antidot diameter and the cyclotron radius, the cyclotron orbit is assumed to pass the constriction at a constant potential $0.6E_F$. This parameter is adapted so that ΔB matches the experiment. Note that ΔB can only be slightly modified by varying this parameter. The slopes with changing s_d are hardly affected at all.

³Note that Gould *et al.* [34] explained the shift of the conductance maxima by the reduced velocity of a particle in the constriction, which also leads to a change of the action of an orbit. The simple AB picture, however, explains already both the spacing of the maxima and their dependence on the antidot diameter. Therefore in this context no additional mechanism has to be introduced.

⁴The electrostatic potential induced by the gates is relatively smooth. The effective single-particle potential, however, gets steeper with increasing particle number. This has been shown in self-consistent calculations for quantum dots [24] and is analogous to the situation in three-dimensional metal clusters [32, 89]. In the limit of high electron densities, the effective potential is box-like. This ensures that the applied gate voltage only determines the depletion region of the gate, whereas the potential steepness depends mainly on the electron density. For the electron densities realized in the experiment, the choice of the model potential consisting of a flat central region with steep walls is justified.

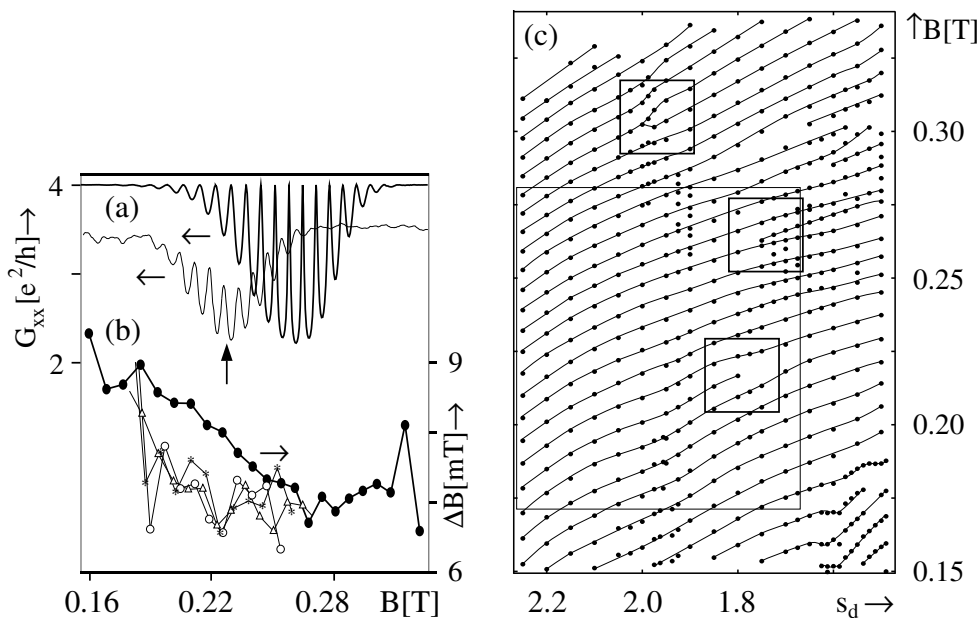


Figure 7.3: *Quantum results. (a) Magnetoconductance. Thick: QM for $s_d = 2.05$, thin: experiment with $V_g = -1.44$ V. The arrow indicates the commensurability condition in the model potential. (b) Spacing of the maxima for $s_d = 2.05$. The thin lines correspond to the experimental curves of Fig. 7.2. (c) Positions of the maxima in dependence of B and s_d . Small boxes indicate dislocations, the large box gives the approximate range of the corresponding experimental data of Fig. 7.2.*

curve. The lack of quantitative agreement could be due to the model potential, whose parameters were not adapted for a perfect fit. Note, however, that the central position of the peak does not coincide with the commensurability condition of the model potential (vertical arrow). The origin of this deviation is unclear.

7.4 Semiclassical description of the conductance

The initial motivation for a semiclassical analysis of this system was to find out whether the variation of the maxima spacings and the dislocations with varying antidot diameter are genuine quantum effects, i. e., of higher than leading order in \hbar . This was claimed in Refs. [48, 34] with two arguments: (1) All classical orbits found by the authors show a dependence of the action S on the magnetic field B which implies a decrease of ΔB with larger B . This contradicts the experimental results. (2) The experiment is performed in the regime of the first plateau of quantized conduction. With just one mode transmitting, a semiclassical approach seems questionable to the authors.

In this chapter, the semiclassical description of the magnetoconductance for the channel system is derived. The results are compared to the quantum mechanical data as well as to the experimental findings. It is discussed why the semiclassical description is – in contrast to the above arguments – able to explain all the experimentally observed features. Thereafter, the lower computational effort of the semiclassical ansatz is used to fit the model potential parameters to the experiment. The close relation of the trace formula to the classical dynamics of the system finally allows to explain all effects within a simple, intuitive picture.

7.4.1 Landauer-Büttiker or Kubo?

Although the quantum mechanical results of the Landauer-Büttiker and the Kubo formalism have shown to be identical [12], the appropriate formulation for a semiclassical approximation has to be chosen.

The Landauer-Büttiker approach [54, 21] is valid for completely phase-coherent devices connected to leads which serve as electron reservoirs. The conductance of such a system can be expressed in terms of the transmission coefficients between all the contact modes. This formalism holds for two-terminal measurements as well as for configurations including more contacts. The channel with central antidots consists of a phase-coherent “active region” (the environment of the antidots), connected by “leads” (the channel itself). Since these leads are not phase coherent (their lengths exceed the phase coherence length), they cannot be considered as part of the device. They are not in thermal equilibrium,⁵ so that they are no contacts in the sense of the Landauer-Büttiker formalism, either. This approach is therefore not applicable to the present system.

The Kubo approach describes the conductivities of homogeneous, macroscopic samples. Since the channel is neither homogeneous nor macroscopic, it is not reasonable to define a conductivity for this system. Nevertheless, the Kubo formalism is applicable. This becomes clear considering a hypothetical system, namely a 2D lattice with the channel system as its elementary cell. This setup is equivalent to the antidot lattices regularly treated within Kubo formalism. The conductivities which are calculated from the Kubo formula refer to the macroscopic dimensions of the (hypothetical) lattice. Since the vertically separated elementary cells can not interfere because of the channel walls, and horizontally separated antidot dimers are further apart as ℓ_{Φ} , the classical scaling laws hold down to a single elementary cell of the lattice, i. e. can be applied to the individual channel with a pair of antidots. The conductance of the individual channel is therefore given by the conductivity in connection with the size of the elementary cell. Since the resistance of the channel itself is negligible, the relevant size is given by the active region, i. e. the region around the antidots.

In the following, the semiclassical version of the Kubo transport formula Eq. (5.4) will be applied to the channel with antidots.

7.4.2 The model potential

To allow a comparison of the results, the quantum mechanical model potential is also used for the semiclassical approach. Numerical stability, however, requires⁶ smooth second derivatives of $V(\mathbf{r})$. The model potential Eq. (7.1) has a discontinuous second derivative between the flat bottom and the quadratic wall. To remove this, a cubic spline is introduced in the transition region. The total potential is given by

$$\frac{V(\tilde{r})}{E_F} = \begin{cases} (|\tilde{r}| - s_1)^2 + \frac{\Delta^2}{12} & |\tilde{r}| < (s_1 - \Delta/2) \\ -\frac{1}{3\Delta}(|\tilde{r}| - s_2)^3 & (s_1 - \Delta/2) < |\tilde{r}| < (s_1 + \Delta/2) \\ 0 & (s_1 + \Delta/2) < |\tilde{r}| \end{cases} \quad (7.2)$$

⁵This is especially clear for high magnetic fields where the current is carried by edge states. The states at the opposite edges of the channel have different Fermi energies in this regime.

⁶This is due to the numerical scheme implemented, which simultaneously integrates the stability matrix. It will be presented in appendix A.

with $\tilde{r} = r/a_0$, $s_1 = 1 + s$ and $\Delta = s_2 - s$. Throughout this chapter, $\Delta = 0.005$ is used. This results in a difference to the pure parabolic case smaller than $2.1 * 10^{-6} E_F$, which is negligible. The potential Eq. (7.2) is illustrated in Fig. 7.4. Unless otherwise noticed,

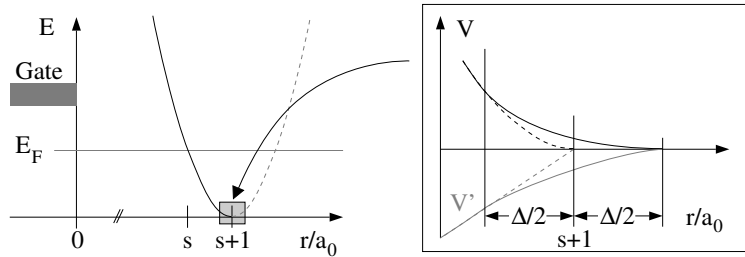


Figure 7.4: *Left: Model potential used for the semiclassical calculations. Right: Closeup of the transition region. Cubic spline correction (solid) and the piecewise parabolic case (dashed).*

the parameters are identical to those of the quantum calculation, i. e. $a_0 = 0.05 \mu\text{m}$ and $s = s_c = 1$ for the gates defining the channel. The depletion width of the antidot gates s_d was varied between 1.5 and 2.2. Following the approximated relation between s_d and V_g in Ref. [48], this corresponds to an effective antidot diameter between $0.35 \mu\text{m}$ and $0.42 \mu\text{m}$.

7.4.3 The periodic orbits

Except for a few special cases, the periodic orbits of a system with smooth potential can only be found numerically. This stage involves the main numerical effort of a semiclassical approximation, so that some care reducing the computation time is indicated. In order not to interrupt the discussion, the corresponding technical (though important) details are given in appendix A. The central idea is to implement a fast numerical differential equation solver to integrate *simultaneously* the classical equations of motion (EOM) and a reduced version of the monodromy matrix, the (2D) stability matrix \tilde{M} . Starting with random initial conditions, a two-dimensional Newton-Raphson iteration using the information provided by \tilde{M} converges to the periodic orbits. These are followed with varying B-field and antidot diameter using an adaptive extrapolation scheme.

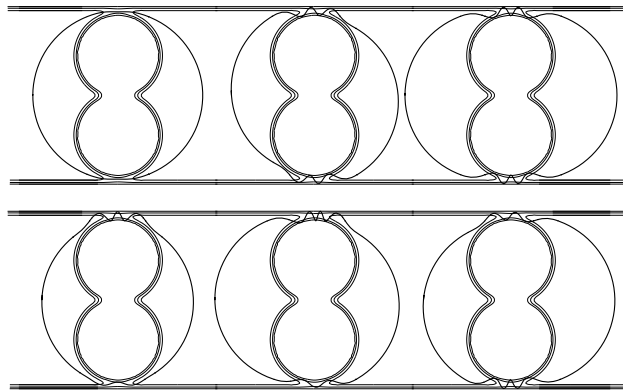


Figure 7.5: *Six typical classical periodic orbits in the channel system. Note that there are orbits breaking the symmetries of the potential.*

Although the potential is simple and symmetric, it gives rise to a large variety of distinct periodic orbits, many of them breaking the symmetry of the system. Some typical examples are shown in Fig. 7.5. According to Sec. 3.2, finite temperature and impurity scattering leads to a strong damping of the contributions of longer periodic orbits to the trace sum. Systems like the disk billiard (see chapter 4) or antidot lattices [63, 41] only have a small number of short periodic orbits. In these cases the evaluation of the semiclassical Kubo formula is especially easy, since only a few contributions are significant. In the channel, unfortunately, the lengths of the orbits are nearly identical, so that much more orbits contribute to the trace sum.

Most of the orbits do not exist over the whole parameter range, appearing and disappearing

in orbit bifurcations. Fig. 7.6 shows the typical behavior of $\text{Tr}(\widetilde{M})$ of some orbits with varying magnetic field. The structure of the classical dynamics is astonishingly rich, showing bifurcations (which correspond to $\text{Tr}(\widetilde{M}) = 2$) of various types and – when varying the antidot diameter s_d – also of higher codimension. The number of orbits increases rapidly with smaller antidot diameter (i. e., wider constriction).

The Poincaré plot of the channel is given in Fig. 7.7. The leftmost picture shows the stability island of a primitive orbit, surrounded by chains of stable and unstable orbits of higher repetition number, in the “sea of chaos”. Varying the magnetic field drives the system through a bifurcation. The central stable orbit becomes unstable, creating a pair of new stable orbits (rightmost picture). This is the typical phase space picture of a period doubling (or pitchfork) bifurcation.

By checking $\text{Tr}(\widetilde{M})$ as in Fig. 7.6, it was ensured that no orbit was missed at a bifurcation. All together, over 60 orbits (not counting the symmetry-related ones) have been included in the calculations. All relevant classical properties, namely the actions, periods, stabilities, velocity-velocity correlation functions, Maslov indices and degeneracies were determined numerically. The technical details are presented in appendix A.2.

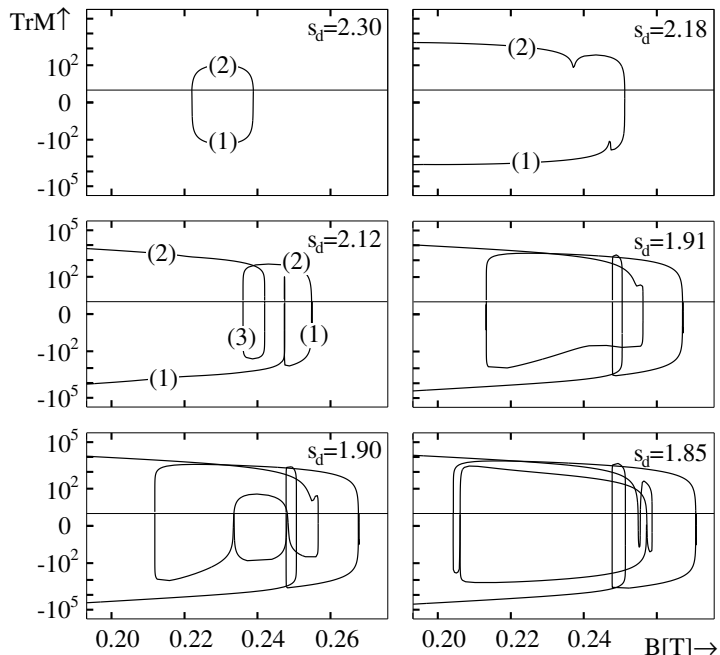


Figure 7.6: The dependence of $\text{Tr}(\widetilde{M})$ of some periodic orbits on B and s_d . The crossings of the line $\text{Tr}(\widetilde{M}) = 2$ indicate bifurcations, where new orbits appear. The number of orbits increases rapidly with smaller antidot diameter s_d . The labels of the orbits refer to a classification in three generations, which will be used in Sec. 7.6.

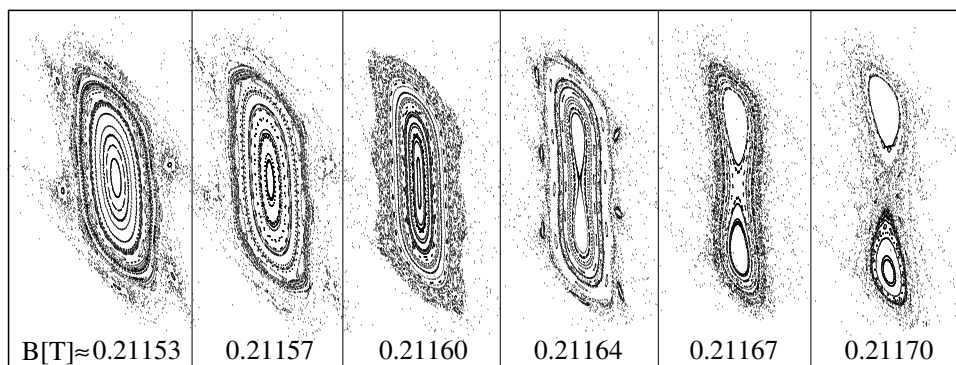


Figure 7.7: Poincaré plot of a small phase-space region for $s_d = 1.9$ for varying B . From left to right: a stable orbit becomes unstable, creating two new stable orbits. The stable orbits are surrounded by chains of stable and unstable orbits with higher repetition number, which is typical for systems with mixed phase space.

7.4.4 Evaluating the trace formula

As discussed in Sec. 2.4, leading-order \hbar approximations diverge at bifurcations. This spurious behavior can be removed by a local higher-order expansion. To ensure both the correct local properties at the bifurcation and the (Gutzwiller-) limit far from it, uniform approximations can be used.

Orbit traces like in Fig. 7.6 allow the identification of the types of bifurcations present in the channel system. Varying the magnetic field both tangent and period doubling bifurcations occur. If additionally the antidot diameter is changed, bifurcations of codimension 2 show up as well. The explicit formulas for the uniform approximation of tangent bifurcations are given in appendix B by Eqs. (B.7) and (B.8). Eq. (B.15) applies to pitchfork bifurcations. The next section deals with the implications that these expressions do not only contain information about the classical periodic orbits, but also include the contribution of *ghost orbits*, i. e., analytic continuations of orbits beyond the regime where they classically exist.

7.4.4.1 Numerical implementation of the uniform approximation

The formulas for the uniform bifurcation cannot be applied directly to the system considered here. First, the channel has discrete symmetries, whereas these formulas apply to the generic, symmetry-free case. The discrete symmetry modifies the behavior of the period doubling bifurcation. Its generic form consists of a central orbit which changes its stability (from stable to unstable or vice versa), splitting off a new orbit with twice the period. In the channel system, in contrast, two symmetry-related orbits with the simple period split off (cf. Fig. 7.7 for a Poincaré plot). The total Gutzwiller amplitudes, however, are identical for the symmetric and the generic situation. The factor 2 from the double period in the generic case is replaced by the degeneracy factor 2 stemming from the symmetry. Including the degeneracies correctly, the uniform approximation of Schomerus and Sieber can be applied to the channel system.

The second problem concerns the numerical implementation of the uniform approximation. The information about the ghost orbits which contribute to the analytical formulation is not available if the classical equations of motion are integrated numerically. This prevents the application of the uniform approximation to the complex side of the bifurcation. This work suggest a modified scheme, which retains the correct limiting cases, but requires only information about real orbits. It consists of a local approximation at the bifurcation, which is adapted to both the local form of the uniform approximation and the limit on the far complex side (which is simply the Gutzwiller contribution of the remaining real orbits). The technical details of the procedure are presented in Appendix B.

7.4.4.2 The influence of the bifurcations

As can be deduced from the analytical local form, the contributions of the orbits engaged in a bifurcation are increased by a factor $\hbar^{-\delta}$. The exponent depends on the type of the bifurcation; for the tangent bifurcation $\delta = 1/6$, and for the period doubling bifurcation $\delta = 1/4$ [70]. This shows that bifurcations are of leading order in \hbar and dominate in the semiclassical limit $\hbar/S \rightarrow 0$ (with S being the action of a typical periodic orbit in the system). Therefore it has to be checked whether the bifurcations have an increased influence on the conductance of the channel system.

Fig. 7.8(a) shows the trace of the (reduced) stability matrix $\text{Tr}(\tilde{M})$ of three periodic orbits taking part in two successive bifurcations (where $\text{Tr}(\tilde{M}) = 2$) under variation of the magnetic field strength B . At $\tilde{B} \approx 0.21$ a tangent bifurcation, and at $\tilde{B} \approx 0.225$ a pitchfork

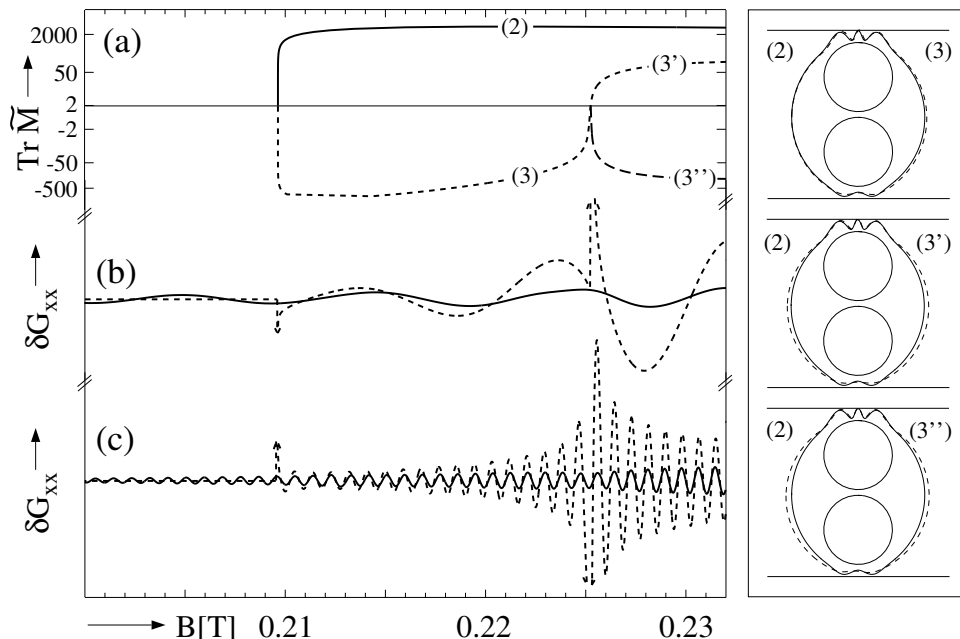


Figure 7.8: (a) $\text{Tr}(\tilde{M})$ (note the nonlinear scale!) versus magnetic field B for three characteristic periodic orbits. (b) Contribution of the three orbits to δG_{xx} ; dotted line: semiclassical Kubo formula, solid line: uniform approximation. (c) same as (b) but for a system with 10 times larger actions. The right box illustrates the orbits engaged in the bifurcations. Note the tiny differences to orbit 2.

bifurcation shows up. Fig. 7.8(b) gives the contribution to the conductance of the orbits engaged in the bifurcations. The dotted line corresponds to the result of the semiclassical Kubo formula Eq. (5.4). The amplitudes are diverging at the bifurcations. The uniform approximation (solid line) removes, as expected, the divergences. Fig. 7.8(c) represents the corresponding data for a system scaled to have 10 times larger actions, thus being closer to the semiclassical limit. Even then, the amplitudes of the uniform approximation are nearly constant over the bifurcations. This shows that the bifurcations have no locally dominant influence on the conductance of the present system.

Having established this result, the semiclassical approximation can be further simplified. Whereas for individual orbits a uniform treatment of the bifurcations is vital, their influence becomes smaller if a larger number of orbits is included. This is demonstrated in Fig. 7.9, where δG_{xx} has been calculated including all relevant (~ 60) periodic orbits. The thin line gives the standard Gutzwiller-like approach in leading order in \hbar according to Eq. (5.4). The sharp divergences correspond to bifurcations of various orbits included in the trace sum. The difference to the uniform result⁷ (solid) is much less pronounced than in Fig. 7.8.

The influence of higher-order \hbar corrections on the result of Gutzwiller-like trace formulae has been discussed in Sec. 3.3. There it was pointed out that \hbar corrections do not only

⁷The numerical uniform approximation was additionally treated with the folding procedure of Sec. 3.3.2 to handle the spurious divergencies stemming from the bifurcations with codimension 2. Those were not included in the numerical uniform approximation.

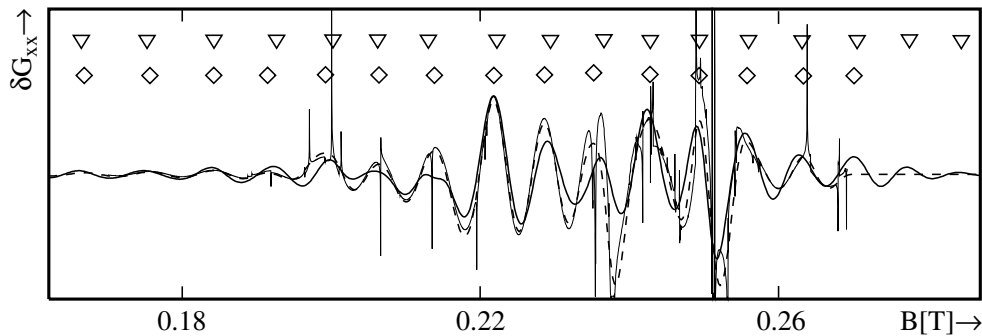


Figure 7.9: δG_{xx} for $s_d = 1.88$ using the semiclassical Kubo formula either directly (thin) or with additional folding over B (dashed). The uniform approximation corresponds to the heavy solid line. Maxima are marked with diamonds (folded Kubo) and triangles (uniform).

lead to additional terms in the trace sum, but also require an adaption of the smoothing scheme. This applies, as pointed out there, also to bifurcations. The correct inclusion of finite temperature and impurity scattering is possible using the folding approach presented in Sec. 3.3.2. This procedure implements the smoothing in higher order in \hbar , but it does not include higher-order \hbar terms to the trace formula. Comparing the uniform approximation with the results of the semiclassical Kubo formula in combination with the folding approach therefore permits an examination of the effects of the higher-order \hbar terms introduced by the bifurcations.

The dashed line in Fig. 7.9 shows the result of the folding approach. It removes the spurious divergencies at the bifurcations, and the remaining discrepancy to the uniform treatment is small. This is in strong contrast to Fig. 7.8, where only a few orbits are included. The semiclassical result therefore depends only little on the correct treatment of the bifurcations if many orbits are included. From this observation it can be deduced that the higher-order \hbar corrections from the different bifurcations interfere mostly destructively. This effect has already been observed in the study of the disk billiard in chapter 4.

In particular, the influence of the bifurcations on the maximum positions (marked by diamonds and triangles in Fig. 7.9) is small. Therefore the semiclassical description can be further simplified by using the trace formula Eq. (5.4) with additional convolution over B . This will be done in the following.

7.5 Semiclassical results

The discussion of the simple Aharonov-Bohm (AB) picture in Sec. 7.3.1 has shown that the observations which still need to be explained are the dependence of the maximum spacings on B , and the dislocations of the maxima positions with varying antidot diameter. This will be discussed in Sec. 7.5.3 and 7.5.4, respectively. Before that, a closer look at the experimental results will be taken.

7.5.1 Fourier components of the quantum oscillations

The semiclassical trace formula Eq. 5.4 has the structure of a Fourier sum, with the periodic orbits as individual Fourier components. If the semiclassical approach is justified

and a formula of this type describes the quantum oscillations, the traces of the classical orbits should be visible in a Fourier transform of the experimental data. This technique has evolved to a standard approach for extracting the influence of the classical phase space structure on quantum oscillations. Prominent calculations of this type include the Rydberg spectrum of hydrogen [92] and of larger atoms [52]. This powerful method shall now be applied to the channel system in order to check whether the quantum oscillations show indications for the influence of classical orbits.

For such an analysis to be rigidly valid, a scaling law for the actions of the periodic orbits must hold. The observed conductance oscillations resemble Aharonov-Bohm oscillations. The action of the corresponding orbits, the cyclotron orbits, scales like $S = \kappa B$. Taking the Fourier transform of G_{xx} with respect to B , orbits with this scaling property show up as sharp peaks. Fig. 7.10 shows Fourier spectra⁸ of the experimental data with respect to B for different antidot voltages. For large antidots (large negative voltage on the antidot gates) one dominant frequency can be observed. With decreasing antidot diameter, the corresponding peak shrinks and finally disappears. Simultaneously, a new peak develops at smaller ΔB . For $V_g \approx -1.24$ V both peaks have approximately equal strength. With decreasing antidot diameter, both peaks move to larger ΔB .

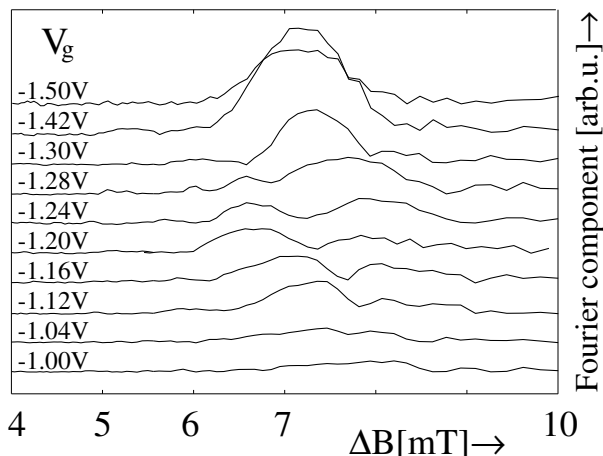


Figure 7.10: *Fourier transform of the experimental data in the range of the commensurability peak $B = 0 \dots 0.5$ T. For easier comparison with Figs. 7.2 and 7.13, the frequency is given in units of the corresponding maxima spacing. Offset for clarity.*

The width of the peaks in Fig. 7.10 is not restricted by the finite resolution of the Fourier transform. This does not necessarily contradict a semiclassical interpretation. The broadening might be caused by orbits whose action scales only approximately like $S = \kappa B$. The widths of the peaks can also be explained by many orbits which contribute, each with a slightly different frequency. The Fourier data therefore neither gives a clear indication of periodic orbits contributing to the quantum oscillation, nor does it exclude this possibility.

The oscillations in G_{xx} seen in experiment (compare to Fig. 7.2) are nearly sinusoidal, so that one might expect that a single periodic orbit is responsible for the effect. The above Fourier analysis of the data shows, however, that at least two orbits contribute to the quantum oscillations.

7.5.2 The conductance variation with B

Fig. 7.11 compares the semiclassical result for the oscillating part of the conductance with the experimental⁹ data.

⁸To clearly separate out the regime of interest around the commensurability peak, a triangular window function was used. The magnetic field range considered was $B = 0 \dots 0.5$ T.

⁹To extract the oscillating part of the conductance from the experimental data, the smooth part was calculated by convolution with a Gaussian with $\sigma = 0.004$ T. The difference to the original data gives δG_{xx} .

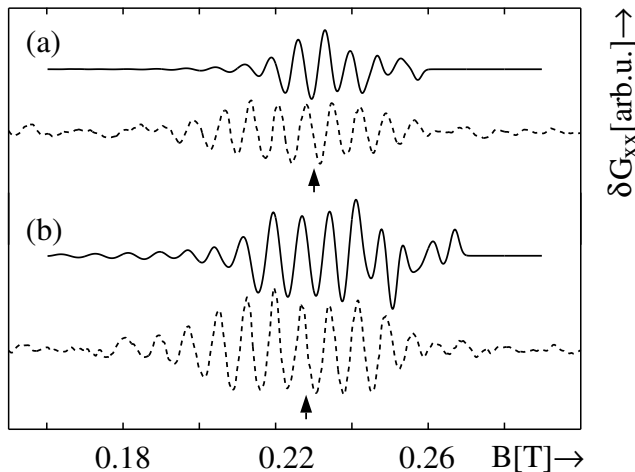


Figure 7.11: Semiclassical (solid) and experimental data (dashed) for δG_{xx} . The arrows indicate the commensurability condition; offset for clarity. (a) Large antidot diameter. Semiclassics: $s_d = 2.06$, experiment: $V_g = -1.48$ V. (b) Intermediate antidot diameter. Semiclassics: $s_d = 1.91$, experiment: $V_g = -1.38$ V.

The semiclassical result shows – apart from small shift towards higher magnetic fields – qualitatively the same behavior as the experimental data. Although using an identical model potential, this shift is considerably smaller than for the quantum calculation (compare to Fig. 7.3). The origin of this discrepancy between the two theoretical descriptions is unclear. Please note in this context that the quantum calculation in contrast to the semiclassical approach does not reproduce the correct position of the classical commensurability peak. This is clear comparing Figs. 7.3 and 7.11, where the commensurability conditions are indicated by vertical arrows.

The numerical effort involved in the semiclassical calculation is considerably smaller than for the quantum approach. It is low enough to make a fit of the model potential to the experimental findings feasible. For this task three parameters of the model system have been varied, namely the overall system size and the depletion widths of the channel and antidot gates, s_c and s_d . Since the classical dynamics are size-independent, the scaling of the system with a factor κ in coordinate space can simply be performed by replacing in Eq. (5.4) the action S with κS and the magnetic field B with $\kappa^{-1}B$. To change s_c , the periodic orbits have to be adapted to the new potential using the same scheme already employed when varying B or s_d (see appendix A.3).

Fig. (7.12) shows the semiclassical conductance for $s_c = 1.5$ and $s_d = 1.5$ for a system scaled with $\kappa = 1.075$, i.e. $s_0 = 0.05375 \mu\text{m}$. This size is still in agreement with the SEM picture Fig. 7.1. The adapted model potential removes the mismatch between the semiclassical and the experimental findings, resulting in a quantitative¹⁰ agreement of the semiclassical δG_{xx} with the experimental data.

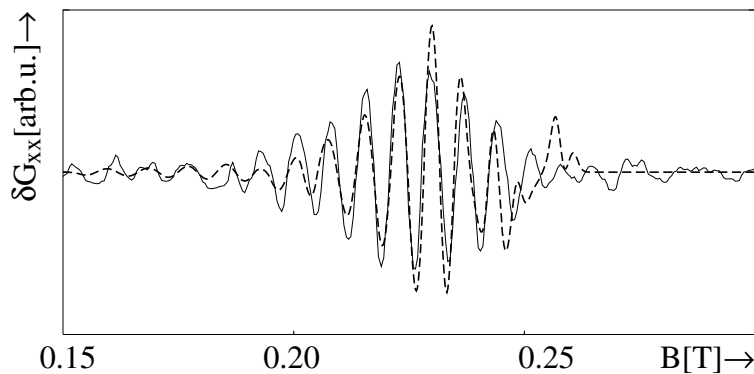


Figure 7.12: Adapting the parameters of the model potential. Solid: experiment for $V_g = -1.50$ V, dashed: semiclassics for $s_c = 1.5$, $s_d = 1.5$, and $s_0 = 0.05375 \mu\text{m}$.

The following calculations return to the parameters of the quantum approach in order to have the two theoretical methods on the same basis.

¹⁰Note that the amplitudes are, as usual in semiclassical calculations, adapted.

7.5.3 The maximum spacing

Fig. 7.13 compares the variation of the maximum spacings of the semiclassical description (heavy lines and filled symbols) to the experimental data¹¹ (thin lines and open symbols). For large (a) as well as for intermediate antidot diameter (b) the average spacing of the maxima is nearly constant in B , only slightly decreasing for stronger fields. This is clearly reproduced by the semiclassical approach. The mean spacing is – both experimentally and in the semiclassical description – unaffected by changes of the antidot diameter. The maxima spacings, however, do not vary smoothly, but show random-like variations for small changes in either B or s_d . Large antidots (Fig. 7.13(a)) give rise to a more regular pattern than smaller antidot diameters (Fig. 7.13(b)). The amount of variation is correctly reproduced by the semiclassical description. The quantum calculation in Fig. 7.3(b) shows less agreement with the experimental data. This is again due to the shift of the quantum G_{xx} to larger magnetic fields, which was already observed in Sec. 7.3.2.

The good agreement of the semiclassical prediction of the maximum spacings with the experimental findings is surprising, since the contributions of the individual orbits show a different behavior. This is illustrated in Fig. 7.14. All individual orbits (thin lines) show a strong decrease of ΔB with stronger fields. This does not agree with the experimental findings for the spacing (heavy lines and symbols). This observation was one of the arguments of Ref. [48], leading to the conclusion that the magnetoconductance of the channel is not accessible to semiclassical approximations. The solution to this apparent contradiction is that in the present system not a few orbits dominate the quantum oscillations, but many of them contribute with comparable amplitudes, actions

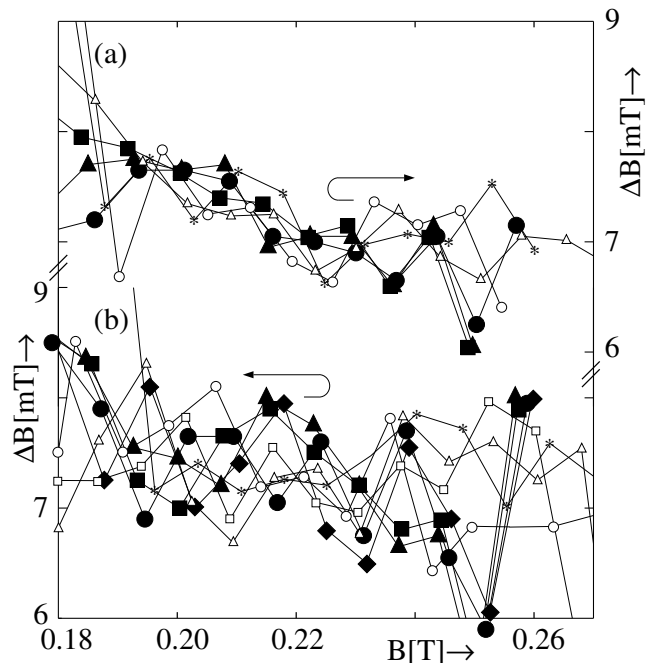


Figure 7.13: *The spacing of the maxima in dependence of B . Thin lines, open symbols: experiment. Heavy lines, filled symbols: semiclassics. (a) Large antidot diameters. Experiment: $V_g = -1.42 \dots -1.5$ V, semiclassics: $s_d = 2.05 \dots 2.07$. (b) Medium antidot diameters. Experiment: $V_g = -1.3 \dots -1.36$ V, semiclassics: $s_d = 1.88 \dots 1.92$.*

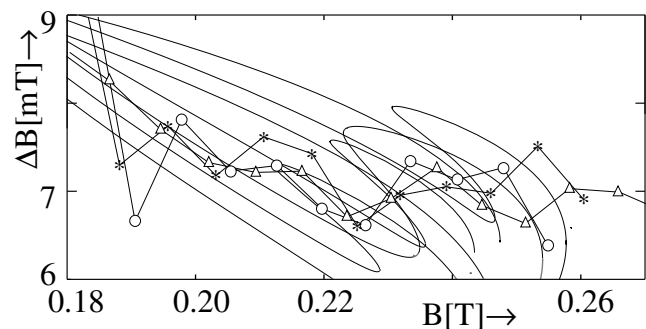


Figure 7.14: *Thick lines and symbols: Experimental maxima spacings as in Fig. 7.13(a). Thin lines: Maxima spacings from the contributions of some individual orbits for $S_d = 2.06$.*

¹¹The maxima positions were determined from the experimental δB . A cubic spline fit was used to interpolate between the measured points. The latter were taken each 0.5 mT.

and periods. Varying the magnetic field, the individual orbits change their ΔB . Simultaneously, the orbit stabilities (and thus the relative amplitudes) are affected. In combination, the two effects lead to the weak variation of ΔB plotted in Fig. 7.13.

The semiclassical analysis is, as depicted in Fig. 7.13, also able to reproduce the amount of short-range variation of the maximum spacings. This shows that the effect is not due to experimental noise, but reflects the physical properties of the system. The basic mechanism can easily be understood within the semiclassical picture. As pointed out above, the influence of the individual orbits varies strongly with both magnetic field and antidot diameter. Small changes in these parameters therefore can lead to significant shifts of the maxima positions. The more the orbits differ geometrically, the larger are the changes in δB induced by tiny changes of the parameters. For larger antidot diameter, i. e. narrow constrictions, the classical orbits get more and more similar to each other. This nicely explains the increased short-range variations of δB for smaller antidots.

Both the sinusoidal form of the experimental δG_{xx} and the Fourier analysis were consistent with the picture that just a few orbits contribute significantly to the trace sum. The analysis of the maxima spacings, however, shows that the idea to trace down the magnetoconductance features to the properties of one or two single orbits must be rejected. The observed behavior depends on the subtle interplay between changes in the classical stabilities and in the actions of a large number of similar orbits.

7.5.4 Variation of the antidot diameter

The second question formulated in Sec. 7.3.1 concerns the dislocations which occur in the positions of the conductance maxima when varying the antidot diameter. Fig. 7.15(a) shows the predictions of the semiclassical approach. The points represent the calculated maxima positions, the thin lines are just a guide for the eye. The semiclassical description clearly reproduces the dislocations (small boxes). This shows that the dislocations are no genuine quantum effect, but accessible by semiclassical methods.

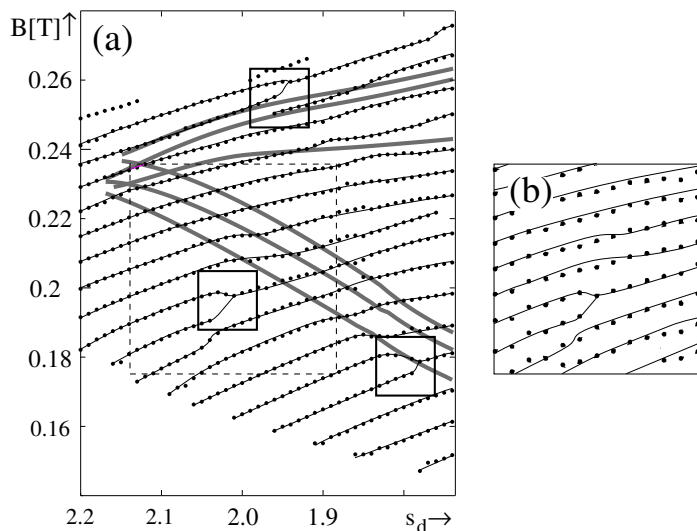


Figure 7.15: (a) Result of the semiclassical analysis for the positions of the conductance maxima with varying magnetic field B and antidot diameter s_d (dots). Thin lines connecting the points are just to guide the eye. The corresponding experimental data is shown in Fig. 7.2. The gray-shaded lines correspond to loci of orbit bifurcations (see Sec. 7.6, p. 86). (b) Local behavior around a dislocation. Lines: semiclassical result of the dashed box in (a), points: experimental data around the dislocation marked with the dashed box in Fig. 7.2.

Fig. 7.15(b) illustrates the local behavior around a dislocation. The lines correspond to the semiclassical result (dashed box in Fig. 7.2(a)), the points give the experimental data of Fig. 7.2(d). The values of B and s_d have been shifted slightly, but no rescaling was used. The excellent agreement shows that the local behavior at a bifurcation is not only qualitatively, but even quantitatively explained within the semiclassical description.

7.6 Semiclassical interpretation

The last section confirmed that the semiclassical approach is able to explain all observed magnetoconductance features of the channel with central antidots. The semiclassical technique has two main advantages compared to quantum calculations. The first benefit, the reduced numerical effort, has already been exploited above. It was therefore possible to calculate the data on a fine grid, and even to adapt the system parameters. Such a task is in principle not impossible in a quantum approach, but frequently the numerical effort is prohibitive.

The second advantage of semiclassical descriptions is that they express quantum oscillations in terms of classical quantities. Since human intuition is strongly based on classical physics, the insight gained in the nature of these interference effects is enlarged by a semiclassical description. The resulting intuitive picture might also be helpful for the development of new devices, serving as a guiding line how to design a sample to achieve certain desired properties. This section exploits the close relation of the trace formula to the classical dynamics of the system to give an intuitive picture of the origin of the maxima dislocations.

The different periodic orbits of the system have different degrees of similarity. A reasonable way of splitting them in groups is to consider always those orbits together which are closely related, i. e., have bifurcations with each other in the parameter range observed. These orbit groups will be called *families*¹². Fig. 7.6 shows the traces of the orbits belonging to such a family, illustrating their close internal relation.

To understand the nature of the effect leading to the dislocations, a model system with only the orbits of this family will be considered for the moment. In Fig. 7.16(c) the squares give the positions of the conductance maxima for this model system. This reduced system already shows all the characteristic features observed in the experiment (see Fig. 7.2). It especially exhibits the dislocations of the conductance maxima (boxes) which are so far reproduced, but unexplained. As illustrated in Fig. 7.6, the members of the family can be divided into three generations, depending on whether an orbit is offspring of the orbit 1, 2 or 3. These are, for obvious reasons, called grandparents, parents, and children generation. All members within a generation behave nearly identical, thus justifying the classification. In Fig. 7.16(a) and (b) the maxima of the contributions of the grandparent and the children generation to the conductance is shown. All generations¹³ induce nearly equidistant maxima in B with a constant shift to larger B if the antidot diameter is reduced. This is in complete agreement with the simple Aharonov-Bohm picture discussed in Sec. 7.3.1. The behavior of the individual generations is therefore readily interpreted in terms of their geometrical properties. This implies, that the contributions of the individual generation do not show dislocations. These must be due to the interplay of the different generations.

The children have a larger semiclassical amplitude than the grandparents. Therefore the maxima of the total G_{xx} (i. e. including all generations) follow the childrens' maxima where the latter exist. Otherwise, the maximum positions of the complete family agree with those of the grandparents. This is confirmed by Fig. 7.16(d). The parents' influence

¹²These families are not to be confused with the families of degenerate orbits occurring in systems with continuous symmetries.

¹³This holds also for the parents generation. It is not shown separately, since its contribution is negligible throughout.

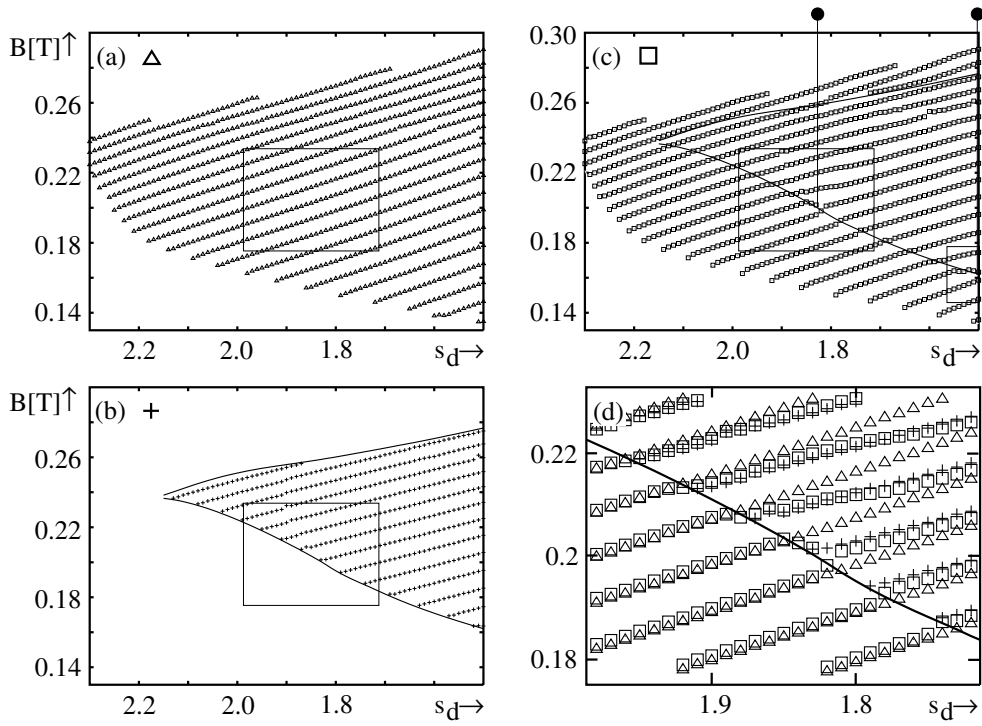


Figure 7.16: The positions of the conductance maxima due to different orbit generations of the family shown in Fig. 7.6: (a) grandparents, (b) children, (c) all generations. The parents' contribution is not shown separately, since it is negligible. (d) Blow-up from (a)-(c). The maxima of the total δG_{xx} (squares) follow the maxima of the children (crosses) where these exist, and those of the grandparents (triangles) otherwise. Heavy lines indicate the loci of bifurcations in the (s_d, B) plane.

was found to be negligible throughout. The geometric differences between grandparents and children orbits lead to different dependencies on the antidot diameter and the magnetic field strengths. Therefore the generations show different maxima spacings as well as different slopes of the maxima with varying s_d . Neither the slopes nor the spacings match along the generation boundaries. This is similar to growing two materials with different lattice constants onto each other. The resulting lattice defects are the equivalent of the dislocations observed.

From this interpretation, further predictions can be deduced: (i) Scaling the system does not affect the classical dynamics, so that the dislocations move along the (universal) bifurcation lines. (ii) Assuming a linear dependence of the action difference ΔS between children and grandparents on s_d , the dislocations are equally spaced in s_d . (iii) Scaling S with a factor κ ,¹⁴ the distances between dislocations scale according to $\Delta s_d \propto \kappa$. These predictions are checked in Fig. 7.17, where the maxima positions of the system of Fig. 7.16(d), scaled with a factor of 2 (a) and 3 (b), are shown. The dislocations move indeed on the bifurcation line. They occur approximately at the predicted values of s_d , which are marked by pins.

In the full calculation with over 60 orbits, the various families with their bifurcation structures (gray lines in Fig. 7.15(c)) are superimposed. Only those dislocations survive for which the above model scenario is locally dominating and no further orbits interfere. As a result, some of the dislocations disappear, some are slightly shifted in the (s_d, B)

¹⁴This corresponds to scaling the size with κ and the magnetic field with κ^{-1} .

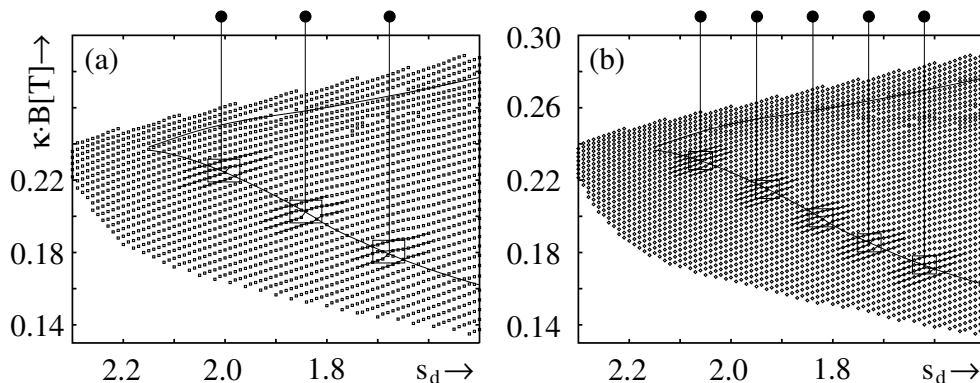


Figure 7.17: *The system of Fig. 7.16(d), scaled by a factor of $\kappa = 2$ (a) and $\kappa = 3$ (b). The thin lines are guide to the eye. The magnetic field is scaled with κ to simplify the comparison with Fig. 7.16. The bifurcation lines (and thus the region where the children exists) are indicated by thick lines. Dislocations are marked with boxes. The pins correspond to the prediction of the location of the dislocations given in the main text.*

plane. Therefore, no unique one-to-one relation between dislocations and bifurcations can be established. Nevertheless, the qualitative pattern remains the same.

This interpretation suggests that there are two orbit groups with different behaviors present, their interplay being responsible for the dislocations of the maxima positions observed. This is in complete agreement with the Fourier analysis of the experimental data shown in Fig. 7.10, which shows two distinct peaks. The Fourier transform of the semiclassical data for the individual orbit generations is given in Fig. 7.18. For large antidot diameter the parents (dashed) have dominant Fourier components, as they exist in a much larger region in B compared to the children (solid). For smaller antidots, the region where children orbits exist rapidly grows, and due to their large semiclassical amplitude they soon dominate the Fourier spectrum. In the intermediate regime, two separate peaks can be observed. This is the same behavior found in the Fourier analysis of the experimental data in Fig. 7.10, where a peak at $\delta B \approx 7\text{mT}$ vanished for smaller antidots, and a new peak occurred. The Fourier analysis of the experimental data therefore supports the interpretation that the observed structure in the maxima positions of the conductance is due to the interplay between two orbit generations.

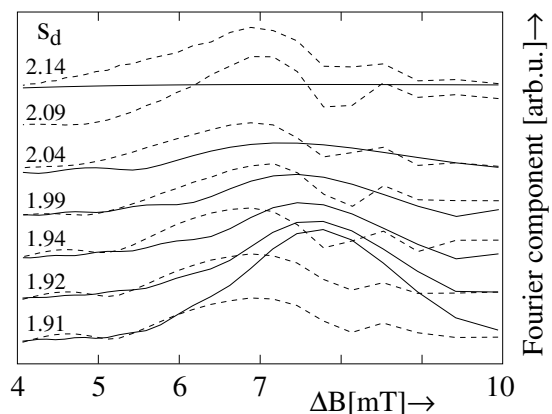


Figure 7.18: *The Fourier transform of the contributions of the individual orbit families. Solid: children, dashed: parents.*

7.7 Summary

In summary, the semiclassical description successfully reproduces all experimentally observed features of the magnetoconductance of a mesoscopic channel with antidots. It was additionally demonstrated that the low numerical demands of the semiclassical approximation make a fit of the experimental potential possible.

The variations in the maxima spacings could be reproduced in every respect. The semiclassical approach yields the correct value for ΔB , together with the average behavior with varying field and antidot diameter. Furthermore, the predictions of the amount of short-range variation of ΔB in dependence of B and s_d agree with the experimental findings. The semiclassical picture confirms that these variations are not due to experimental inaccuracies, but reflect system properties.

The dislocations of the conductance maxima as functions of magnetic field B and antidot diameter s_d have been shown to be related to bifurcations of the leading classical periodic orbits of the system. The dislocations are due to the fact that the bifurcations define the border lines between regimes of different predominant orbit generations, leading to different dependences of the conductance maxima on B and s_d . This induces the observed dislocations of the maximum positions, analogously to lattice defects at interfaces. As the classical dynamics are not affected by a rescaling of the system, the scaling behavior of the dislocations can be easily understood in the semiclassical approach.

These results disprove previous arguments claiming the channel system exhibits inherent quantum features. These arguments were based on the discussion of the semiclassical contributions of *individual* orbits. The semiclassical picture proposed here, in contrast, claims that the subtle interplay between many different orbits, i. e. the variations in all their stabilities and actions under the change of the system parameters, is responsible for the observed magnetoconductance features.

The way how bifurcations affect the quantum oscillations in the channel system is different from previously reported mechanisms. Using a numerical version of uniform approximations, the bifurcations of the system were shown to have no locally enhanced influence on the conductance. In super-deformed nuclei [10] or elliptic billiards [57], in contrast, period doubling orbit bifurcations influence the quantum shell structure due to their dominant order in $1/\hbar$. The influence of the bifurcations in the present system is also different from the one reported for the resonant tunneling diode [114]. There, the bifurcations lead to a doubling of the period, whereas in the system considered here the periods of all relevant orbits are approximately constant. Furthermore, in the resonant tunneling diode only a few orbits were found to be important, whereas the present system is dominated by a much larger number of orbits with nearly identical actions, periods and amplitudes.